
**Nested-grid
simulation of
mercury over North
America**

Y. Zhang et al.

[Title Page](#)[Abstract](#)[Introduction](#)[Conclusions](#)[References](#)[Tables](#)[Figures](#)[I◀](#)[▶I](#)[◀](#)[▶](#)[Back](#)[Close](#)[Full Screen / Esc](#)[Printer-friendly Version](#)[Interactive Discussion](#)

¹³ Environment Canada, Air Quality Research Division, Toronto, Ontario, Canada

¹⁴ Department of Microbiology and Environmental Toxicology, University of California, Santa Cruz, CA, USA

¹⁵ Division of Environmental Regulation, Bureau of Air Quality Monitoring, New Jersey Department of Environmental Protection, Trenton, NJ, USA

Received: 20 December 2011 – Accepted: 18 January 2012 – Published: 26 January 2012

Correspondence to: Y. Zhang (yanxuz@atmos.washington.edu)

Published by Copernicus Publications on behalf of the European Geosciences Union.

Abstract

We have developed a new high-resolution ($1/2^\circ$ latitude by $2/3^\circ$ longitude) nested-grid mercury (Hg) simulation over North America employing the GEOS-Chem global chemical transport model. Emissions, chemistry, deposition, and meteorology are self-consistent between the global and nested domains. Compared to the global model (4° latitude by 5° longitude), the nested model shows improved skill at capturing the high spatial and temporal variability of Hg wet deposition over North America observed by the Mercury Deposition Network (MDN) in 2008–2009. The nested simulation resolves features such as land/ocean contrast and higher deposition due to orographic precipitation, and predicts more efficient convective rain scavenging of Hg over the southeast United States. However, the nested model overestimates Hg wet deposition over the Ohio River Valley region (ORV) by 27%. We modify anthropogenic emission speciation profiles in the US EPA National Emission Inventory (NEI) to account for the rapid in-plume reduction of reactive to elemental Hg (IPR simulation). This leads to a decrease in the model bias to +3% over the ORV region. Over the contiguous US, the correlation coefficient (r) between MDN observations and our IPR simulation increases from 0.63 to 0.78. The IPR nested simulation generally reproduces the seasonal cycle in surface concentrations of speciated Hg from the Atmospheric Mercury Network (AMNet) and Canadian Atmospheric Mercury Network (CAMNet). In the IPR simulation, annual mean reactive gaseous and particulate-bound Hg are within 80% and 10% of observations, respectively. In contrast, the simulation with unmodified anthropogenic Hg speciation profiles overestimates these observations by factors of 2 to 4. The nested model shows improved skill at capturing the horizontal variability of Hg observed over California during the ARCTAS aircraft campaign. We find that North American anthropogenic emissions account for 10–22% of Hg wet deposition flux over the US, depending on the anthropogenic emissions speciation profile assumed. The percent contribution can be as high as 60% near large point emission sources in ORV. The contribution for the dry deposition is 13–20%.

Nested-grid simulation of mercury over North America

Y. Zhang et al.

Title Page

Abstract

Introduction

Conclusions

References

Tables

Figures



Back

Close

Full Screen / Esc

Printer-friendly Version

Interactive Discussion



1 Introduction

Mercury (Hg) is a ubiquitous trace metal in the atmosphere and is emitted by both natural (Mason, 2009) and anthropogenic sources such as coal combustion, waste incineration and gold mining (Streets et al., 2009; Pacyna et al., 2010). Anthropogenic emissions of Hg occur in the long-lived elemental form (Hg^0), but also as short-lived oxidized mercury (Hg^{II}) and particulate-bound mercury (Hg_p). Both Hg^{II} and Hg_p are rapidly removed by wet and dry deposition near source regions, while Hg^0 can be transported on global scales. Hg^0 is then deposited over remote areas via dry deposition of Hg^0 itself or through oxidation to Hg^{II} , followed by its subsequent deposition (Lindberg et al., 2007). Once in aquatic ecosystems, Hg may be converted to the neurotoxin methylmercury, which can bioaccumulate in the food chain (Morel et al., 1998). Human exposure occurs via consumption of fish and seafood (Mergler et al., 2007; Sunderland, 2007).

A number of global Hg models have been developed to interpret observations, test chemical mechanisms and constrain the global Hg budget (e.g. GISS-CTM: Shia et al., 1999; GEOS-Chem: Selin et al., 2007; GRAHM: Dastoor and Larocque, 2004) (Strode et al., 2008). However, these models often have coarse horizontal resolution ($\sim 200\text{--}1000\text{ km}$) and thus lack the resolution needed for detailed evaluation at the regional scale. Regional models have high resolution over a limited domain, which is necessary to resolve the observed high spatial variability in Hg deposition (Keeler et al., 2006; Dvonch et al., 2005). A disadvantage of these models is their sensitivity to assumed initial and lateral boundary conditions. One way to solve this issue is to use a global model to provide initial and boundary conditions in a multi-scale modeling approach (Bash, 2010; Bullock et al., 2008; Lin and Tao, 2003; Pan et al., 2007; Seigneur et al., 2001; Vijayaraghavan et al., 2008). A significant problem with this approach, however, is that the regional and global models often use different assumptions about Hg emissions, chemistry, deposition, and meteorology. Use of different global models to define boundary conditions leads to large variations in regional patterns of atmospheric Hg concentrations, as well as wet and dry deposition (Bullock et al., 2008, 2009).

Nested-grid simulation of mercury over North America

Y. Zhang et al.

Title Page

Abstract

Introduction

Conclusions

References

Tables

Figures



Back

Close

Full Screen / Esc

Printer-friendly Version

Interactive Discussion



**Nested-grid
simulation of
mercury over North
America**Y. Zhang et al.

[Title Page](#)[Abstract](#)[Introduction](#)[Conclusions](#)[References](#)[Tables](#)[Figures](#)[⏪](#)[⏩](#)[◀](#)[▶](#)[Back](#)[Close](#)[Full Screen / Esc](#)[Printer-friendly Version](#)[Interactive Discussion](#)

The GEOS-Chem atmospheric Hg simulation is described and evaluated in Selin et al. (2007), with recent updates in Hg chemistry and deposition by Holmes et al. (2010) and Amos et al. (2012). The model includes three atmospheric mercury species: Hg^0 , Hg^{II} , and primary particulate Hg from anthropogenic sources (Hg_p). Anthropogenic Hg emissions are from the Global Emission Inventory Activity (GEIA) 2005 inventory of Pacyna et al. (2010), with a native spatial resolution of $0.5 \times 0.5^\circ$. The resulting global anthropogenic emissions are 1900 Mg a^{-1} . Natural sources account for a total of $6,600 \text{ Mg a}^{-1}$, including 4900 Mg a^{-1} (2900 Mg a^{-1} net evasion) from air-sea exchange (Strode et al., 2007; Soerensen et al., 2010), 1400 Mg a^{-1} from land (Selin et al., 2008; Amos et al., 2012), 220 Mg a^{-1} from open fire biomass burning (Global Fire Emission Database version 2, assuming Hg/CO emission ratio as 100 nmol/mol suggested by Holmes et al., 2010), and 130 Mg a^{-1} from snow re-emissions (Holmes et al., 2010).

Considerable uncertainty remains on the Hg^0 oxidation mechanisms and their kinetics (Gårdfeldt et al., 2001; Calvert and Lindberg, 2005; Si and Ariya, 2008). In the original GEOS-Chem simulation, Selin et al. (2007) assumed OH and O_3 to be the main oxidants for Hg^0 . They also included aqueous-phase photochemical reduction of Hg^{II} , proportional to OH concentrations and scaled to match constraints on Hg lifetime and seasonal variation. Holmes et al. (2010) updated GEOS-Chem to use Br atoms as the sole oxidant for Hg^0 , with kinetic parameters from Donohoue et al. (2006), Goodsite et al. (2004) and Balabanov et al. (2005). They found that Hg + Br chemistry, like the previous Hg + OH/ O_3 chemistry, can reproduce most mercury observations, with some improved prediction of the interhemispheric gradient in total gaseous mercury (TGM) concentrations and the TGM concentrations in polar regions. Holmes et al. (2010) included aqueous-phase photochemical reduction of Hg^{II} , scaled to NO_2 photolysis. We follow the Holmes et al. (2010) chemical mechanism in this work.

The global bromine fields are described in Holmes et al. (2010), and are based on 3-D monthly archived Br concentrations from the p-TOMCAT model in the troposphere (Yang et al., 2005) and from NASA's Global Modeling Initiative model in the stratosphere (Strahan et al., 2007). Over polar regions, elevated concentrations of Br atoms

can be produced by refreezing of open leads during spring (Simpson et al., 2007), leading to so-called bromine explosion events and rapid depletion of Hg^0 (Steffen et al., 2008). This process is parameterized by assuming 5 ppt BrO in the polar boundary layer during springtime over areas with sea ice, sunlight, stable conditions and temperatures below 268 K.

GEOS-Chem simulates wet scavenging of Hg^{II} and Hg_p and dry deposition of Hg^0 , Hg^{II} , and Hg_p following the scheme of Liu et al. (2001) and the resistance-in-series scheme of Wesely (1989), respectively. When deposition is calculated, the Hg^{II} tracer is assumed to be partitioned between gaseous and particulate phases based on the empirical relationship developed by Amos et al. (2012). We also assume complete retention of Hg^{II} and Hg_p during freezing of supercooled water in mixed-phase clouds, but no scavenging during vapor condensation to cloud ice (Holmes et al., 2010; Wang et al., 2011). Below-cloud scavenging by snow is included only for Hg^{II} in the aerosol phase and Hg_p (Holmes et al., 2010; Amos et al., 2012). The loss of Hg^{II} via uptake onto sea-salt aerosol and subsequent deposition in the marine boundary layer is also included in this study (Holmes et al., 2009, 2010).

2.2 Nested-grid Hg simulation

We have implemented a new high-resolution nested-grid capability in the GEOS-Chem Hg simulation. We use results from the global ($4 \times 5^\circ$) Hg simulation as initial and boundary conditions for a nested-grid simulation over North America (10° – 70° N and 40° – 140° W). The nested model is driven by GEOS-5 meteorological fields at their native horizontal resolution ($1/2 \times 2/3^\circ$). This one-way nesting approach was first developed in GEOS-Chem by Wang et al. (2004a, b) to examine CO and NO_x variability over Asia, and has also been applied to understand ozone and aerosol chemistry over North America (Fiore et al., 2005; Li et al., 2005; Park et al., 2006). These simulations used an earlier version of the GEOS fields (GEOS-3) with a native resolution of $1 \times 1^\circ$. More recently, Chen et al. (2009) updated the nested-grid CO simulation over Asia to use the newest GEOS-5 data, allowing for higher resolution. Chen et al. (2009) found

Nested-grid simulation of mercury over North America

Y. Zhang et al.

[Title Page](#)[Abstract](#)[Introduction](#)[Conclusions](#)[References](#)[Tables](#)[Figures](#)[⏪](#)[⏩](#)[◀](#)[▶](#)[Back](#)[Close](#)[Full Screen / Esc](#)[Printer-friendly Version](#)[Interactive Discussion](#)

that the higher spatial resolution allows for more efficient advection-related ventilation of the lower atmosphere and can better resolve frontal lifting. The nested model can also resolve the variability of emission densities over individual cities.

We first conducted a global $4 \times 5^\circ$ resolution simulation (referred to as the global model) for 2004–2009, archiving tracer mixing ratios of Hg^0 , Hg^{II} and Hg_p at the lateral boundaries of the nested model every 3 h. The nested model was then run for 2008–2009 using these 3-hourly lateral mixing ratios, with an initial spin-up time of one month starting with initial conditions from the global model. Figure 1 (top panels) compares the meteorological data driving the global and nested models, using precipitation as an example. The nested model resolves many fine features in the spatial distribution of precipitation which are lost by horizontal averaging at the $4 \times 5^\circ$ resolution. In particular, orographic precipitation is identifiable in the mountain ranges along the west coast of North America, the Rocky Mountains and the Appalachian Mountains. In addition, details in precipitation over the Gulf of Mexico and Northwest Atlantic are more clearly apparent.

Anthropogenic Hg emissions in the US were obtained from the 2005 EPA NEI inventory (NEI05, <http://www.epa.gov/ttn/chief/eiinformation.html>). The NEI05 inventory includes Hg emissions from point, nonpoint (area), and mobile sources within different sectors. We assign the point source Hg emissions into the corresponding model grid box according to geographic location. For nonpoint and mobile sources, the county-specific Hg emissions were distributed into the model grid system with the surrogate data provided by the EPA (<http://www.epa.gov/ttn/chief/emch/spatial/newsurrogate.html>). Mercury speciation profiles are reported for all coal-fired power plants (CFPPs) individually in the NEI05 inventory. For other sources, we use the source-specific emission profiles reported in the inventory. Over the continental US, the 2005 anthropogenic Hg emissions are 111.3 Mg a^{-1} ($61.5 \text{ Mg a}^{-1} \text{ Hg}^0$, $39.3 \text{ Mg a}^{-1} \text{ Hg}^{\text{II}}$, $10.5 \text{ Mg a}^{-1} \text{ Hg}_p$). Point sources dominate these emissions with 104.7 Mg a^{-1} , while nonpoint and mobile sources emit 5.5 Mg a^{-1} and 1.1 Mg a^{-1} , respectively. CFPPs account for 49% of the total national anthropogenic emissions.

Nested-grid simulation of mercury over North America

Y. Zhang et al.

Title Page

Abstract

Introduction

Conclusions

References

Tables

Figures

⏪

⏩

◀

▶

Back

Close

Full Screen / Esc

Printer-friendly Version

Interactive Discussion



Nested-grid simulation of mercury over North America

Y. Zhang et al.

Title Page

Abstract

Introduction

Conclusions

References

Tables

Figures

⏪

⏩

◀

▶

Back

Close

Full Screen / Esc

Printer-friendly Version

Interactive Discussion



Over Canada, we used emissions from the Canadian National Pollutant Release Inventory 2005 (NPRI05, <http://www.ec.gc.ca/inrp-npri/>). The point sources in the NPRI05 inventory were processed in a similar manner as those in NEI2005, and the area and mobile sources were spatially allocated over the model grid using population as the surrogate. The total Canadian anthropogenic Hg emissions are 6.2 Mg a^{-1} ($3.8 \text{ Mg a}^{-1} \text{ Hg}^0$, $1.4 \text{ Mg a}^{-1} \text{ Hg}^{\text{II}}$, $1.0 \text{ Mg a}^{-1} \text{ Hg}_P$). Anthropogenic emissions from Mexico in the nested model domain are directly gridded from the GEIA emission inventory, and account for 27.9 Mg a^{-1} .

Observations collected at ground-based sites 7–15 km downwind of power plants in the Southeastern US show that Hg^{II} accounts for only 8–21 % of total Hg (Edgerton et al., 2006; Weiss-Penzias et al., 2011). This is a factor of ~ 3 –5 lower than the Hg^{II} fraction measured in CFPPs stacks (40–70 % Hg^{II}). From airborne measurements downwind of a CFPP, ter Schure et al. (2011) show that reduction occurs in CFPP plumes much faster than in the background atmosphere. Vijayaraghavan et al. (2008) incorporated this rapid reduction into a regional Hg model with an explicit treatment of stack plume evolution. They found that this improved model performance for wet deposition in the Northeast US. In order to consider this process in our study, we modified the CFPPs Hg emission partitioning from the original 56.8 % Hg^0 , 39.6 % Hg^{II} , 3.6 % Hg_P in the NEI and NPRI inventories to 86.5 % Hg^0 , 9.9 % Hg^{II} , 3.6 % Hg_P over the US and Canada. This effectively assumes that 75 % of the CFPPs Hg^{II} emissions are reduced to Hg^0 in the immediate vicinity of power plants, consistent with the Edgerton et al. (2006) and Weiss-Penzias et al. (2011). Furthermore the NEI inventory assumes relatively high portions of Hg^{II} and Hg_P in the emission profiles for waste incineration (22 % Hg^0 , 58 % Hg^{II} , 20 % Hg_P). We assume a similar in-plume reduction process happens to this source, and replaced the speciation profile by 96 % Hg^0 , 0 % Hg^{II} , 4 % Hg_P (Streets et al., 2009).

With these speciation profile changes, the resulting anthropogenic Hg emissions in North America are: $122 \text{ Mg a}^{-1} \text{ Hg}^0$, $18 \text{ Mg a}^{-1} \text{ Hg}^{\text{II}}$ and $6 \text{ Mg a}^{-1} \text{ Hg}_P$. We will refer to simulations with this inventory as in-plume reduction (IPR) simulations and contrast

them to our standard (STD) simulations with the original anthropogenic Hg speciation ($87 \text{ Mg a}^{-1} \text{ Hg}^0$, $46 \text{ Mg a}^{-1} \text{ Hg}^{\text{II}}$ and $13 \text{ Mg a}^{-1} \text{ Hg}_\text{P}$ over North America). To have self-consistent global and North American anthropogenic inventories in the IPR simulation, we also modified the $\text{Hg}^0:\text{Hg}^{\text{II}}:\text{Hg}_\text{P}$ speciation profile for fossil fuel combustion in Pa-

cyna et al. (2010) from 50:40:10 to 86.5:9.9:3.6 (Amos et al., 2012).
Figure 1 (bottom panels) shows the spatial distribution of total anthropogenic Hg emissions over North America. These are held constant over the 2008–2009 simulation period. Emissions are highest in coal combustion regions in the Ohio River Valley and eastern Texas. Some individual point sources such as power plants and municipal waste incinerators are distinct in the nested model, whereas they are averaged over much larger regions in the global model.

Within the nested model domain the following emissions are interpolated to fine resolution from the global model: geogenic (60 Mg a^{-1}), legacy soil (130 Mg a^{-1}). Other emissions are calculated interactively within the nested model using the same algorithms as the global model, including biomass burning (10 Mg a^{-1}), oceans (260 Mg a^{-1}), soil (33 Mg a^{-1}), and snow (11 Mg a^{-1}). Figure 1 (middle panels) shows the total Hg emission from both anthropogenic and natural sources. Geogenic Hg emissions are a significant source in western North America along a band stretching from southwest Canada to Mexico (Gustin et al., 1997). The re-emissions from soil, snow and ocean generally follow the spatial pattern of anthropogenic emissions. Soil, snow and ocean emissions strengths depend on meteorology, but vary by less than 15% over these two years.

The monthly concentrations of Br, BrO and OH radicals in the nested model are obtained by interpolating fields used in the global model. To evaluate the contribution from North American anthropogenic, we conducted a sensitivity study with primary anthropogenic emissions from the US, Canada and Mexico turned off. We will refer to this simulation as the “background” simulation.

Nested-grid simulation of mercury over North America

Y. Zhang et al.

Title Page

Abstract

Introduction

Conclusions

References

Tables

Figures

⏪

⏩

◀

▶

Back

Close

Full Screen / Esc

Printer-friendly Version

Interactive Discussion

3 Model evaluation

We evaluated the nested-grid model against a series of observations in North America including Hg wet deposition from the Mercury Deposition Network (MDN, 2011), near surface Hg concentrations from the Atmospheric Mercury Network (AMNet, 2009) and from the Canadian Atmospheric Mercury Measurement Network (CAMNet, 2011), and tropospheric Hg concentrations observed during the ARCTAS aircraft campaign (Mao et al., 2011). We will also compare the nested model against the global model.

3.1 Annual mean Hg wet deposition

Figure 2 shows the 2008–2009 annual mean Hg wet deposition flux over North America predicted by the global (upper panel) and nested (middle panel) models for the STD simulation. The eastern US is divided as MW (Midwest), NE (Northeast), ORV (Ohio River Valley and Mid-Atlantic), and SE (Southeast) as shown in Fig. 2. The spatial distribution of wet deposition is the result of the combined variations of anthropogenic Hg^{II} emissions, free tropospheric Hg^{II} concentrations and precipitation. Although the global model and the nested model have very similar large scale patterns for wet deposition, the nested model resolves more detail (Fig. 2). In the nested model, high wet deposition fluxes occur along the coastal regions of British Columbia, Washington and Mexico due to orographic precipitation; discrete high wet deposition flux is predicted over the Rocky Mountains following precipitation (Fig. 1). Higher spatial variability is also predicted by the nested model near point sources over the ORV and SE regions. For instance, the global model shows the highest wet deposition occurring over the grid box covering southern Indiana, Kentucky and southern Ohio. In contrast, the nested model shows elevated wet deposition flux concentrated over eastern Ohio and western Pennsylvania. Furthermore, the nested model can resolve the land/ocean contrast in coastal regions (e.g. Florida and the western Gulf Coast) and predicts higher wet deposition flux over land due to higher updraft velocity (Mari et al., 2000). With this improvement, the nested model is able to reproduce the observed latitudinal pattern for

Nested-grid simulation of mercury over North America

Y. Zhang et al.

Title Page

Abstract

Introduction

Conclusions

References

Tables

Figures

⏪

⏩

◀

▶

Back

Close

Full Screen / Esc

Printer-friendly Version

Interactive Discussion



Hg wet deposition over the SE region – the deposition flux increases with lower latitude – which is totally smoothed out by the coarse global model.

Figure 2 also displays Hg wet deposition flux measurements from the MDN network (circles). MDN sites collect weekly integrated precipitation samples and report Hg wet deposition flux and the Hg concentration in precipitation (MDN, 2011). Here we use the annual mean wet deposition flux for 2008–2009 for MDN sites with at least 75 % of annual data availability (95 sites are selected). One issue with the samplers used by MDN is their low snow collection efficiency (Butler et al., 2008; Prestbo and Gay, 2009). Prestbo and Gay (2009) find that the MDN annual collection efficiency of precipitation is $87.1 \pm 6.5\%$ at cold weather sites, but is unbiased at warm weather sites (efficiency = $98.8 \pm 4.3\%$). Lynch et al. (2003) summarized the 16 sites in Pennsylvania in 2002 and found the average collection efficiencies was 89 % in the cold period when snow and/or ice dominate precipitation. We correct for this bias in MDN weekly wet deposition by taking into account the fraction of annual precipitation falling as snow and assuming an 89 % collection efficiency of snow. The resulting annual wet deposition increases by 2 % at sites in the NE and MW regions, with an 11 % increase in winter. Wet deposition over the ORV and SE (where snow accounts for 11 % and <2 % of annual precipitation, respectively) are nearly unaffected. All the MDN observations we show in this paper are corrected for this snow bias.

The standard nested-grid simulation captures the general spatial pattern of MDN wet deposition, especially the east-west gradient and higher wet deposition flux over the SE region (Fig. 2). However, the standard model systematically overestimates the observed wet deposition flux over the ORV region. As shown in Table 1, the mean normalized model bias is +27 % in this region. For all 95 MDN sites, the model displays a +3 % bias with a correlation coefficient $r = 0.63$ (Fig. 3 left). The sites with the largest positive model bias are in ORV (blue circles), while negative model bias primarily occurs in the SE (orange circles) and the central and western US (denoted as OT, purple circles). Calculated regionally, the correlation coefficients vary drastically, and are largest over the OT region ($r = 0.79$, Fig. 3), lowest in ORV ($r = 0.17$).

**Nested-grid
simulation of
mercury over North
America**

Y. Zhang et al.

Title Page

Abstract

Introduction

Conclusions

References

Tables

Figures



Back

Close

Full Screen / Esc

Printer-friendly Version

Interactive Discussion



Nested-grid simulation of mercury over North America

Y. Zhang et al.

Title Page

Abstract

Introduction

Conclusions

References

Tables

Figures

⏪

⏩

◀

▶

Back

Close

Full Screen / Esc

Printer-friendly Version

Interactive Discussion



When we change the partitioning of anthropogenic Hg emissions in our IPR simulation (Sect. 2.2), the simulated Hg wet deposition flux in the ORV region is reduced by 20 % (Fig. 2, bottom panel). In particular for Athens, Ohio (OH02) the model bias decreases from 200 % to 23 % (Fig. 3). There are several major power plants located near this site that have a total of more than $0.5 \text{ Mg a}^{-1} \text{ Hg}^{\text{II}}$ emission in the corresponding $1/2 \times 2/3^\circ$ model grid. This accounts for 3 % of the total power plant Hg^{II} emission of the US in the standard NEI2005 inventory. Smaller decreases occur over the NE (13 %), MW (17 %), and SE (9 %) regions, and nearly no change in the western and central US due to the smaller Hg contribution from anthropogenic emissions. The IPR simulation leads to improved agreement with MDN observations over the ORV region, with a decrease in the model bias from +27 % to +3 % (Table 1) accompanied by an increase in the correlation coefficient from 0.17 to 0.62 (Fig. 3). Over the MW, NE and SE regions the correlation coefficients improve, however the mean bias tends to worsen somewhat in the IPR simulation (MW from -15% to -28% ; NE from $+2.6 \%$ to -11% ; SE from -14% to -20% , Table 1). As discussed in Sect. 3.2 some of the low bias in the IPR simulation is associated with seasonal underestimates in precipitation for these regions. The overall correlation coefficient for all the MDN sites increases from $r = 0.63$ to $r = 0.78$. For 70 % of the MDN sites, IPR model values are within $\pm 25 \%$ of observations.

Vijayaraghavan et al. (2008) conducted a more complex plume-in-grid modeling of the reduction of Hg^{II} in the plumes and found 10–30 % reduction in wet deposition over the ORV region, partially correcting their overprediction of wet deposition in that region. Our results are consistent with this previous study.

3.2 Seasonal variations in Hg wet deposition

The observed Hg wet deposition flux has a strong seasonality in the eastern US, with a peak during summer and minimum during winter (Fig. 4). The STD simulation generally captures this seasonality. The STD simulation overestimates observed mean Hg wet

deposition over the ORV region throughout the year (red line in Fig. 4, upper panels), but this overestimate disappears in the IPR simulation (green line). The GEOS-5 meteorological fields reproduce monthly precipitation observations in both the ORV and NE regions quite well (bottom panels in Fig. 4; Table 1). The annual mean low bias of the IPR simulation for the MW region is associated with a 50 % underestimate of wet deposition during June and July. This seems to be partially caused by an underestimate in precipitation (30 %) during this time.

Over the SE, the IPR simulation underestimates MDN observations from August to October. While the model reproduces the high deposition rates observed over Louisiana, Mississippi, and Alabama, it does not reproduce the very high wet deposition rates ($10\text{--}12\ \mu\text{g m}^{-2}\ \text{season}^{-1}$) observed at sites in Florida (Fig. 5). During summer, the model meteorological fields capture the observed high precipitation rates observed in the SE ($15\text{--}20\ \text{cm month}^{-1}$) due to convective precipitation. The high wet deposition rates in the SE, especially over Florida, have been attributed to deep convective scavenging from the free troposphere (Guentzel et al., 2001; Selin and Jacob, 2008). Thus the modeled low bias during late summer and autumn over Florida might be due to errors in the height of deep convection or to an underestimate of Hg^{II} concentration in the tropical free atmosphere (Holmes et al., 2010).

Figure 5 shows the spatial distribution of the Hg wet deposition flux for each season. The IPR nested simulation and MDN observations are plotted separately. In winter (December, January, February (DJF)), the observed wet deposition flux is highest over the SE, in a region extending from Louisiana to Tennessee. Deposition rates increase in spring (March, April, May (MAM)) with high deposition areas extending northward to the MW. During summer (June, July, August (JJA)), wet deposition is very high along the Gulf Coast in a region covering eastern Texas to Florida, and further stretches to the NE. During autumn (September, October, November (SON)), the observed wet deposition decreases again and has similar spatial distribution to that of winter. Generally, the nested model captures the change in the spatial pattern of wet deposition among seasons very well (Figs. 5 and 6). The correlation coefficient varies between

Nested-grid simulation of mercury over North America

Y. Zhang et al.

Title Page

Abstract

Introduction

Conclusions

References

Tables

Figures

⏪

⏩

◀

▶

Back

Close

Full Screen / Esc

Printer-friendly Version

Interactive Discussion

$r = 0.69$ (JJA) and $r = 0.77$ (MAM). The IPR nested-grid simulation has the greatest predicting capacity over the eastern US during spring in terms of both low mean bias and correlation coefficient. During summer, the nested model captures the observed maximum high deposition fluxes over the SE, but underestimates MDN observations over the MW, as noted above. The nested model also underestimates the observed high deposition fluxes in SE in autumn and winter.

3.3 Annual mean surface concentrations of atmospheric Hg

Figure 7 shows the annual mean (2008–2009) TGM, reactive gaseous mercury (RGM) and particulate-bound mercury (PBM) surface concentrations for the IPR Hg simulation. The primary refractory Hg_p is treated as Hg^{II} and is lumped together with Hg^{II} following Amos et al. (2012). RGM and PBM in the model are the $\text{Hg}^{\text{II}} + \text{Hg}_p$ in the gaseous and particulate phases, respectively. TGM in the model is calculated as the sum of Hg^0 and RGM.

The global and nested simulations show similar spatial distribution patterns for surface Hg concentrations following natural and anthropogenic Hg emissions. High TGM concentrations are predicted over the ORV region ($1.7\text{--}1.8 \text{ ng m}^{-3}$), where a large number of power plants and waste incinerators are located. Elevated TGM concentrations ($1.5\text{--}1.6 \text{ ng m}^{-3}$) also occur in Nevada and Utah where metal ore smelting plants (NEI05) and strong geogenic sources are located (Gustin et al., 1997). TGM concentrations are lower ($1.3\text{--}1.5 \text{ ng m}^{-3}$) over the Great Plains region, southern Canada and northern Mexico, corresponding to typical Northern Hemisphere background concentrations (Temme et al., 2003; Lindberg et al., 2007). The TGM concentrations are also generally lower ($1.2\text{--}1.4 \text{ ng m}^{-3}$) in the marine boundary layer (MBL) because of lower emissions (Fig. 1, middle panels).

Compared with TGM, both RGM and PBM display stronger variability due to their much shorter lifetimes. Following the anthropogenic emission pattern, RGM and PBM concentrations are enhanced over the ORV region ($10\text{--}20 \text{ pg m}^{-3}$), and are lowest in

Nested-grid simulation of mercury over North America

Y. Zhang et al.

[Title Page](#)[Abstract](#)[Introduction](#)[Conclusions](#)[References](#)[Tables](#)[Figures](#)[⏪](#)[⏩](#)[◀](#)[▶](#)[Back](#)[Close](#)[Full Screen / Esc](#)[Printer-friendly Version](#)[Interactive Discussion](#)

the region stretching across Southern Canada, the Great Plains, southern Canada and northern Mexico. The RGM surface concentrations are highest over the West because of the subsidence of free tropospheric air (Selin and Jacob, 2008). The simulated PBM concentrations are low in this region because of the low particulate matter concentrations.

As expected, the nested model reveals much more spatial variability than the global model, especially near large point sources and over western North America. The average surface RGM and PBM concentrations in the nested model are 40 % higher than in the global model. This is due to the stronger ventilation of surface air in the nested model, which more efficiently mixes Hg^{II} -rich free tropospheric air down to the surface. The global model averages the sub-grid vertical velocity and suppresses subsidence of Hg^{II} from higher altitude (Wang et al., 2004), where Hg^{II} concentrations are high due to faster oxidation of Hg^0 at lower temperatures and lack of removal (Holmes et al., 2010).

We compare the model results to surface concentrations measured at 5 CAMNet sites and 14 AMNet sites (Figs. 7 and 8). CAMNet was established in 1996 and measures TGM across Canada using Tekran mercury vapor analyzers (Temme et al., 2007). AMNet is part of the National Atmospheric Deposition Program and currently consists of 20 sites (AMNET, 2009). Hg measurements are also conducted by Tekran instruments, and include Hg^0 , RGM and PBM with a 2.5-micrometer impactor and KCl-coated annular denuder (for ionic Hg), thermally-desorbed particulate filter (for PBM), and gold traps (for Hg^0). For model evaluation, we have selected 14 sites which are not influenced by large nearby sources (sites with $<2000 \text{ kg a}^{-1}$ anthropogenic Hg emissions within 100 km).

The nested IPR simulation reproduces the observed TGM annual mean concentrations at the 19 surface sites with no bias (obs.: $1.46 \pm 0.11 \text{ ng m}^{-3}$, IPR model: $1.47 \pm 0.11 \text{ ng m}^{-3}$). Observed PBM concentrations are well-captured by the IPR simulation (obs.: $8.4 \pm 4.8 \text{ pg m}^{-3}$, IPR model: $7.1 \pm 5.6 \text{ pg m}^{-3}$), however the model tends to overestimate observed RGM concentrations by 80 % (obs.: $6.8 \pm 4.7 \text{ pg m}^{-3}$, IPR

Nested-grid simulation of mercury over North America

Y. Zhang et al.

Title Page

Abstract

Introduction

Conclusions

References

Tables

Figures

⏪

⏩

◀

▶

Back

Close

Full Screen / Esc

Printer-friendly Version

Interactive Discussion



model: $12 \pm 7.0 \text{ pg m}^{-3}$). If we take into account the large variability ($\pm 70\%$) and high uncertainty (30–40%) in RGM measurements (Aspmo et al., 2005; Lyman et al., 2007; Gustin and Jaffe, 2010) this degree of agreement is not unreasonable, especially since the model has some success at reproducing the seasonal cycle of RGM observations (see Sect. 3.4).

The nested model shows higher correlation ($r = 0.52, 0.64$ and 0.51 for TGM, RGM and PBM, respectively, for IPR simulation) with observations than does the global model ($r = 0.44, 0.26$ and 0.47 , respectively). Indeed, for the NE region, where the number density of AMNet sites is highest, the nested model captures the north-south gradient much better than the global model, such as higher TGM concentrations in the Bronx (NY06, 1.52 ng m^{-3}) than in upstate New York (NY43 and NY49, $1.42\text{--}1.33 \text{ ng m}^{-3}$).

The STD nested simulation predicts RGM and PBM concentrations that are twice as great as the IPR simulation; furthermore, the STD simulation overestimates observations by a factor of 4 for RGM (obs.: $6.8 \pm 4.7 \text{ pg m}^{-3}$, STD model: $26 \pm 24 \text{ pg m}^{-3}$) and 2 for PBM (obs.: $8.4 \pm 4.8 \text{ pg m}^{-3}$, STD model: $16 \pm 18 \text{ pg m}^{-3}$). This indicates a high sensitivity of RGM and PBM concentrations to local Hg^{II} emissions and shows that the AMNet RGM and PBM observations are consistent with rapid reduction of RGM in CFPPs plumes.

3.4 Seasonal variation of surface Hg concentrations

Figure 8 compares the seasonal cycle of observed and modeled TGM, RGM and PBM surface concentrations at AMNet and CAMNet sites. The observations at CAMNet sites are averaged over 2004–2007 (top four panels). For each AMNet site, the range of years with available observations is indicated in Fig. 8. The nested model results (STD: red line; IPR: green line) are averaged over 2008–2009.

The model closely matches the seasonal cycle of TGM at sites that are farthest from anthropogenic point sources. These include Kejimkujik, Burnt Island, NY20, VT99. At

Nested-grid simulation of mercury over North America

Y. Zhang et al.

[Title Page](#)[Abstract](#)[Introduction](#)[Conclusions](#)[References](#)[Tables](#)[Figures](#)[⏪](#)[⏩](#)[◀](#)[▶](#)[Back](#)[Close](#)[Full Screen / Esc](#)[Printer-friendly Version](#)[Interactive Discussion](#)

Nested-grid simulation of mercury over North America

Y. Zhang et al.

Title Page

Abstract

Introduction

Conclusions

References

Tables

Figures

⏪

⏩

◀

▶

Back

Close

Full Screen / Esc

Printer-friendly Version

Interactive Discussion



these sites, the seasonal cycle exhibits a summer minimum, which the model attributes to stronger oxidation and deposition in summer (Bergan and Rodhe, 2001; Selin et al., 2007; Holmes et al., 2010). Discrepancies between observations and models seem to occur when sites are affected by local sources (Kellerhals et al., 2003). For example, Chester, New Jersey (NJ32), Rochester, New York (NY43), and Antelope Island, Utah (UT96). The remote site in Kejimikujik, Nova Scotia shows a TGM maximum in June with a high standard deviation, indicating episodic influence by long range transport and/or fires.

The observed seasonal cycles for RGM vary from site to site. Most of the sites have a maximum during spring and a minimum during summer (e.g. MD08, NH06, NJ32, NS01, NY06, NY43, NY95 and VT99), while other sites (e.g. MS12, MS99 and UT96) show a maximum in summer. Similar site-to-site variability in the RGM seasonality was noted by Engle et al. (2010). These variations are likely caused by different combinations of the seasonality for oxidation, deposition, and subsidence of upper troposphere/lower stratospheric (UT/LS) air at these sites (Amos et al., 2012): oxidation is strongest in late spring, wet deposition is strongest during summer, and UT/LS influence maximizes in winter-spring. The IPR simulation captures the summer-time maximum of RGM at MS12 and UT96. However, it predicts little seasonality at the other sites and does not capture the spring-time peak observed at most of the sites. The reasons for this are unclear at this point, but could be associated with an underestimate of subsidence of RGM-rich air during spring.

The AMNet sites show a much closer clustering in the seasonal cycle for PBM with higher concentration in the colder months, when Hg^{II} would be expected to preferentially partition to aerosols (Rutter and Schauer, 2007; Amos et al., 2012). The IPR simulation captures this seasonality rather well, especially at the sites in New Jersey, New York, and Vermont (NJ32, NY06, NY20, NY43, NY95, and VT99).

3.5 Vertical and horizontal variations of TGM over California during ARCTAS

Figure 9 shows the vertical distribution of TGM obtained in summer 2008 during the ARCTAS aircraft campaign (Jacob et al., 2010). We focus here on observations collected during flights over California and Nevada (32° – 43° N, 114° – 125° W), originating at the Palmdale and Moffett Field (CA) Airports. The measurements include Hg^0 and some fraction of Hg^{II} due to uncertain inlet loss of Hg^{II} (Holmes et al., 2010), so for comparison to the GEOS-Chem nested IPR simulation we show both the Hg^0 and TGM vertical profiles. We exclude episodic biomass burning plumes from the observations ($\text{CO} > 200$ ppb or $\text{CH}_3\text{CN} > 0.25$ ppt following Holmes et al., 2010). The nested IPR simulation is sampled at the same time and altitude as the ARCTAS aircraft observations. The nested simulation reproduces the observed mean TGM concentration below 2 km altitude (1.1 – 1.3 ng m^{-3}). Above 2 km altitude, observations show a slight increase to 1.3 ng m^{-3} . This is not captured by the model, which shows a relatively invariant vertical profile. Overall, the nested model shows no significant bias (Hg^0 : 1.16 ng m^{-3} ; TGM: 1.25 ng m^{-3}) compared with observations (1.21 ng m^{-3}).

The spatial distribution of observed TGM concentrations is displayed in Fig. 10. We show the modeled TGM concentrations from the global and nested IPR simulations for comparison. Because the model shows much smaller variability than the observations, we use different color scales and mainly focus on the relative spatial patterns. Although both the global and nested models have similar level of correlation ($r = 0.3$) with ARCTAS observations, the nested model shows improved skill at capturing the spatial variability in observations. The nested model simulates localized enhancements in TGM over fires sampled in northern California (the branch with red color near 30° – 40° N and 122° W in the right panel). It also captures higher TGM concentrations due to anthropogenic emissions in southern California near Los Angeles. The global model shows weaker and diluted enhancement of concentrations in these regions. Both the global and nested models miss the observed high concentration in western Nevada, which might be caused by a mix of mining activities and naturally Hg-enriched soils (Lyman and Gustin, 2008).

Nested-grid simulation of mercury over North America

Y. Zhang et al.

Title Page

Abstract

Introduction

Conclusions

References

Tables

Figures

⏪

⏩

◀

▶

Back

Close

Full Screen / Esc

Printer-friendly Version

Interactive Discussion



3.6 Origin of Hg deposition over North America

We conduct a sensitivity study where all anthropogenic emissions over the US, Canada, and Mexico are turned off to separate the influence on deposition of regional anthropogenic Hg emissions from background emissions.

The two left panels in Fig. 11 show annual mean wet deposition over North America contributed by background sources (natural sources over North America as well as all sources outside of North America) for the STD and IPR simulations. These external sources lead to a maximum in wet deposition stretching from southern Texas to the NE. There is also a maximum over Florida. These two simulations predict nearly identical spatial distributions. The IPR simulation predicts slightly (5%) higher background wet deposition than the STD simulation. Indeed the IPR simulation assumes that a lower fraction of anthropogenic emissions as Hg^{II} and Hg_P , leading to increased export efficiency of anthropogenic emissions from regions outside of North America.

The contribution from anthropogenic North American Hg emissions is obtained by difference between this background simulation and simulations including anthropogenic emissions (central and right panels in Fig. 11). As expected, the assumed speciation of anthropogenic Hg emissions greatly affects our results. In the STD simulation, we find that North American anthropogenic sources account for 22% of the Hg wet deposition flux and 20% of the dry deposition flux in the contiguous United States, respectively (Table 2). North American anthropogenic sources are responsible for large contributions in the industrial ORV, MW and NE (~30% of wet deposition), with the contributions near the borders between Ohio, Pennsylvania and West Virginia reaching up to 60% (Fig. 11). The contribution from North America anthropogenic sources decreases gradually away from this region. In our IPR simulation we find that the contribution of anthropogenic North American emissions to wet deposition decreases by a factor of 2 relative to the STD simulation (Table 2): 10% of wet deposition and 13% of dry deposition in the contiguous US (compared to 22% and 20% in the STD simulation), reaching a maximum of 15% (wet) and 24% (dry) in the ORV region (compare to 32% and 41% in the STD simulation).

Nested-grid simulation of mercury over North America

Y. Zhang et al.

Title Page

Abstract

Introduction

Conclusions

References

Tables

Figures

⏪

⏩

◀

▶

Back

Close

Full Screen / Esc

Printer-friendly Version

Interactive Discussion



Nested-grid simulation of mercury over North America

Y. Zhang et al.

[Title Page](#)

[Abstract](#)

[Introduction](#)

[Conclusions](#)

[References](#)

[Tables](#)

[Figures](#)

[⏪](#)

[⏩](#)

[◀](#)

[▶](#)

[Back](#)

[Close](#)

[Full Screen / Esc](#)

[Printer-friendly Version](#)

[Interactive Discussion](#)



A similar diagnosis was done by Selin and Jacob (2008) with OH/O₃ as the main oxidants of Hg using GEOS-Chem at a spatial resolution of 4 × 5°. They found the North American anthropogenic sources account for 27 % and 17 % for the wet and dry deposition fluxes over contiguous US, respectively. Seigneur et al. (2004) used the regional model TEAM at a resolution of 100 km and found North American emissions contributions to deposition to be 24 % (wet) and 43 % (dry). The results for wet deposition from both studies are similar to results from our STD simulation which assumes a high fraction of anthropogenic emissions as Hg^{II}. For example, Selin and Jacob (2008) assume anthropogenic emissions of 55 Mg a⁻¹ Hg^{II} and 23 Mg a⁻¹ Hg_P for the year 2000 over North America, similar to our STD emission inventory (46 Mg a⁻¹ Hg^{II} and 13 Mg a⁻¹ Hg_P for 2005). Seigneur et al. (2004) assume 72 Mg a⁻¹ Hg^{II} and 13 Mg a⁻¹ Hg_P (for years 1998–1999). Our IPR simulation assumes significantly lower emissions for Hg^{II} (18 Mg a⁻¹) and Hg_P (6.0 Mg a⁻¹), leading to a decrease in Hg deposition near point sources, and thus a decrease in their contribution to the deposition flux over the contiguous US. This implies that the domestic contribution diagnosed by this approach is highly sensitive to the large uncertainties associated with anthropogenic Hg emission speciation and in-plume reduction processes. Given the improved agreement of our IPR simulation with observations of wet deposition (Sects. 3.1 and 3.2), RGM and PBM (Sect. 3.4), our 12 % estimate of the North American anthropogenic contribution to deposition appears to be most consistent with observations.

Compared to the model results of Selin and Jacob (2008) our results differ in the spatial distribution of background sources' contribution to wet deposition. Selin and Jacob (2008) calculated a maximum wet deposition flux over southern Texas of 18–20 μg m⁻², nearly twice as large as our 10–12 μg m⁻². Compared to Br atom oxidation, the OH/O₃ chemistry shifts wet deposition to tropical regions with elevated OH concentrations (Holmes et al., 2010). Convective precipitation in the GEOS-4 meteorological fields is stronger than in the GEOS-5 fields. In addition, the updates for Hg wet deposition implemented by Wang et al. (2011) and Amos et al. (2012) could also influence the spatial distribution of Hg wet deposition flux.

Nested-grid simulation of mercury over North America

Y. Zhang et al.

Title Page

Abstract

Introduction

Conclusions

References

Tables

Figures

⏪

⏩

◀

▶

Back

Close

Full Screen / Esc

Printer-friendly Version

Interactive Discussion



Many studies have tried to estimate the contribution of local sources to wet deposition, either using surface observations or models. In general, estimates that relied on observations result in higher contributions than estimated by models. Keeler et al. (2006) attributed ~70 % of Hg wet deposition at Steubenville, Ohio to coal combustion. In a later study, White et al. (2009) found an enhancement of up to 72 % of Hg concentration in precipitation at sites within 1 km of power plants during episodic events, and 42 % when averaged over the whole summer season. Similar studies conducted in the Chicago/Gary urban area show that sites less than 100 km apart differed in volume-weighted mean Hg concentration by over 30 % (Lin and Pehkonen, 1999). The volume-weighted mean Hg concentration measured in urban sites in Detroit was also 25–35 % higher than those measured in a rural site ~60 km east (Gildemiester, 2001). The short lifetimes of Hg^{II} and Hg_P lead to strong spatial variance near point sources at a spatial scale of 1–10 km, which cannot be captured in our GEOS-Chem nested grid simulation with a ~50 km horizontal resolution.

4 Conclusions

We have developed a nested Hg simulation in the GEOS-Chem chemical transport model, with a horizontal resolution of 1/2° latitude by 2/3° longitude over North America. Boundary conditions are provided by a global GEOS-Chem Hg simulation at 4 × 5° resolution using the same emissions, chemistry, deposition, and meteorological fields as the high-resolution nested model.

We have updated the anthropogenic Hg emission in the US and Canada using the EPA's National Emissions Inventory and the Canadian National Pollutant Release Inventory, both for 2005. The resulting anthropogenic Hg emissions in North America are 87 Mg a⁻¹ Hg⁰, 46 Mg a⁻¹ Hg^{II} and 13 Mg a⁻¹ Hg_P. While these inventories assume that a significant fraction of anthropogenic emissions are emitted as Hg^{II} (~40 %), observations in power plant plumes suggest that most of this Hg^{II} is quickly reduced to Hg⁰ directly downwind. We therefore conduct a sensitivity simulation where we change

the anthropogenic Hg speciation profile over North America to yield $122 \text{ Mg a}^{-1} \text{ Hg}^0$, $18.0 \text{ Mg a}^{-1} \text{ Hg}^2$ and $6.0 \text{ Mg a}^{-1} \text{ Hg}_p$. We contrast results from this in-plume reduction (IPR) simulation to our standard (STD) simulation.

Relative to the global model, the high-resolution nested-grid model shows improved skill at capturing the high spatial and temporal variability of Hg wet deposition observed at MDN sites. However, the standard nested model simulation shows a systematic 27% overestimate in Hg wet deposition over the Ohio River Valley (ORV), a region with high emissions from coal-fired power plants in the NEI inventory. Changing the speciation of anthropogenic emissions in our IPR simulation reduces this overestimate to 3% over the ORV region, and improves the model performance over North America. The IPR simulation also captures the spatial patterns of wet deposition as a function of season, with high wet deposition fluxes concentrated in the SE during spring and extending towards the NE during summer. The IPR simulation shows a 50% underestimate in wet deposition over the MW in summer associated with a 30% underestimate in precipitation. While the model reproduces the high deposition rates observed in the SE in Louisiana, Mississippi, and Alabama, it does not reproduce the very high wet deposition rates ($10\text{--}12 \mu\text{g m}^{-2} \text{ season}^{-1}$) observed at sites in Florida during summer (June–August).

The nested IPR simulation reproduces the observed annual mean and seasonal variations in surface concentrations of TGM, RGM and PBM observed at 5 CAMNet sites and 14 AMNet sites. The nested model reproduces the horizontal variability in observations better than the global model, because it better resolves the influence of local anthropogenic sources. The nested IPR model shows no bias for TGM and PBM, but is 80% too high relative to RGM observations. In contrast, the STD simulation leads to a factor of 2–4 overestimate in observed RGM and RGP. This may be further evidence for rapid in-plume reduction of RGM. The nested model captures the overall horizontal variability in TGM concentrations observed over California during the ARCTAS campaign, but displays a reduced dynamic range compared to observations.

Nested-grid simulation of mercury over North America

Y. Zhang et al.

Title Page

Abstract

Introduction

Conclusions

References

Tables

Figures

⏪

⏩

◀

▶

Back

Close

Full Screen / Esc

Printer-friendly Version

Interactive Discussion



Nested-grid simulation of mercury over North America

Y. Zhang et al.

Title Page

Abstract

Introduction

Conclusions

References

Tables

Figures

⏪

⏩

◀

▶

Back

Close

Full Screen / Esc

Printer-friendly Version

Interactive Discussion



By conducting a sensitivity study without the North American anthropogenic Hg emissions, we assess the relative contribution of regional anthropogenic emissions on wet deposition. Our results are highly sensitive to the assumed speciation of anthropogenic emissions. In the IPR simulation, the North American anthropogenic sources contributes only 10 % of the total Hg wet deposition in the US, compared to 22 % in the STD simulation. The percent contribution varies from 4 % in the western US to 16 % (32 % in the STD simulation) in the eastern US. The percent contribution can be as high as 60 % near some large point emission sources. The mean contribution of North American anthropogenic emissions to dry deposition is 13 % (20 % in the STD simulation), increasing to 24 % in the Ohio River Valley (41 % in the STD simulation). Given the improved agreement with wet deposition, RGM, and RGP observations obtained in the IPR simulation, our lower estimate of North American contribution to deposition (12 %) appears to be more robust.

Acknowledgements. This work was supported by funding from EPRI under contract EP-35343/C16024. We thank EPRI program manager Leonard Levin for his support during this study. We would like to acknowledge and thank all the site operators for the CAMNet, AMNet, and MDN networks.

References

- AMNet, NADP's Atmospheric Mercury Network: Moving toward Total Mercury Deposition, National Atmospheric Deposition Program, Illinois State Water Survey, Champaign, IL, available at: <http://nadp.sws.uiuc.edu/amn/>, 2009.
- Amos, H. M., Jacob, D. J., Holmes, C. D., Fisher, J. A., Wang, Q., Yantosca, R. M., Corbitt, E. S., Galarneau, E., Rutter, A. P., Gustin, M. S., Steffen, A., Schauer, J. J., Graydon, J. A., Louis, V. L. St., Talbot, R. W., Edgerton, E. S., Zhang, Y., and Sunderland, E. M.: Gas-particle partitioning of atmospheric Hg(II) and its effect on global mercury deposition, *Atmos. Chem. Phys.*, 12, 591–603, doi:10.5194/acp-12-591-2012, 2012.
- Aspmo, K., Gauchard, P., Steffen, A., Temme, C., Berg, T., Bahlmann, E., Banic, C., Dommergue, A., Ebinghaus, R., and Ferrari, C.: Measurements of atmospheric mercury species

- during an international study of mercury depletion events at Ny-Ålesund, Svalbard, spring 2003. How reproducible are our present methods?, *Atmos. Environ.*, 39, 7607–7619, 2005.
- Balabanov, N. B., Shepler, B. C., and Peterson, K. A.: Accurate global potential energy surface and reaction dynamics for the ground state of HgBr₂, *J. Phys. Chem. A*, 109, 8765–8773, 2005.
- Bash, J. O.: Description and initial simulation of a dynamic bidirectional air-surface exchange model for mercury in Community Multiscale Air Quality (CMAQ) model, *J. Geophys. Res.*, 115, D0635, doi:10.1029/2009JD012834, 2010.
- Bergan, T. and Rodhe, H.: Oxidation of elemental mercury in the atmosphere; Constraints imposed by global scale modelling, *J. Atmos. Chem.*, 40, 191–212, 2001.
- Bey, I., Jacob, D. J., Yantosca, R. M., Logan, J. A., Field, B. D., Fiore, A. M., Li, Q. B., Liu, H. G. Y., Mickley, L. J., and Schultz, M. G.: Global modeling of tropospheric chemistry with assimilated meteorology: Model description and evaluation, *J. Geophys. Res.*, 106, 23073–23095, 2001.
- Bullock, O. R., Atkinson, D., Braverman, T., Civerolo, K., Dastoor, A., Davignon, D., Ku, J.-Y., Lohman, K., Myers, T. C., Park, R. J., Seigneur, C., Selin, N. E., Sistla, G., and Vijayaraghavan, K.: The North American Mercury Model Intercomparison Study (NAMMIS): Study description and model-to-model comparisons, *J. Geophys. Res.*, 113, D17310, doi:10.1029/2008JD009803, 2008.
- Bullock, O. R., Atkinson, D., Braverman, T., Civerolo, K., Dastoor, A., Davignon, D., Ku, J. Y., Lohman, K., Myers, T. C., Park, R. J., Seigneur, C., Selin, N. E., Sistla, G., and Vijayaraghavan, K.: An analysis of simulated wet deposition of mercury from the North American Mercury Model Intercomparison Study, *J. Geophys. Res.*, 114, D08301, doi:10.1029/2008jd011224, 2009.
- Butler, T. J., Cohen, M. D., Vermeylen, F. M., Likens, G. E., Schmeltz, D., and Artz, R. S.: Regional precipitation mercury trends in the eastern USA, 1998–2005: Declines in the Northeast and Midwest, no trend in the Southeast, *Atmos. Environ.*, 42, 1582–1592, 2008.
- Calvert, J. G. and Lindberg, S. E.: Mechanisms of mercury removal by O₃ and OH in the atmosphere, *Atmos. Environ.*, 39, 3355–3367, 2005.
- CAMNet, Canadian Atmospheric Mercury Measurement Network, Environment Canada, available at: http://www.msc.ec.gc.ca/arqp/camnet_e.cfm, last access: October 2011.
- Chen, D., Wang, Y., McElroy, M. B., He, K., Yantosca, R. M., and Le Sager, P.: Regional CO pollution and export in China simulated by the high-resolution nested-grid GEOS-Chem

Nested-grid simulation of mercury over North America

Y. Zhang et al.

Title Page

Abstract

Introduction

Conclusions

References

Tables

Figures

◀

▶

◀

▶

Back

Close

Full Screen / Esc

Printer-friendly Version

Interactive Discussion



**Nested-grid
simulation of
mercury over North
America**

Y. Zhang et al.

[Title Page](#)[Abstract](#)[Introduction](#)[Conclusions](#)[References](#)[Tables](#)[Figures](#)[⏪](#)[⏩](#)[◀](#)[▶](#)[Back](#)[Close](#)[Full Screen / Esc](#)[Printer-friendly Version](#)[Interactive Discussion](#)

model, *Atmos. Chem. Phys.*, 9, 3825–3839, doi:10.5194/acp-9-3825-2009, 2009.

Dastoor, A. and Larocque, Y.: Global circulation of atmospheric mercury: a modelling study, *Atmos. Environ.*, 38, 147–161, 2004.

Donohoue, D. L., Bauer, D., Cossairt, B., and Hynes, A. J.: Temperature and pressure dependent rate coefficients for the reaction of Hg with Br and the reaction of Br with Br: A pulsed laser photolysis-pulsed laser induced fluorescence study, *J. Phys. Chem. A*, 110, 6623–6632, 2006.

Dvornch, J. T., Keeler, G. J., and Marsik, F. J.: The influence of meteorological conditions on the wet deposition of mercury in southern Florida, *J. Appl. Meteorol.*, 44, 1421–1435, 2005.

Edgerton, E. S., Hartsell, B. E., and Jansen, J. J.: Mercury speciation in coal-fired power plant plumes observed at three surface sites in the southeastern US, *Environ. Sci. Technol.*, 40, 4563–4570, 2006.

Engle, M. A., Tate, M. T., Krabbenhoft, D. P., Schauer, J. J., Kolker, A., Shanley, J. B., and Bothner, M. H.: Comparison of atmospheric mercury speciation and deposition at nine sites across central and eastern North America, *J. Geophys. Res.*, 115, D18306, doi:10.1029/2010jd014064, 2010.

Fiore, A. M., Horowitz, L. W., Purves, D. W., Levy, H., Evans, M. J., Wang, Y. X., Li, Q. B., and Yantosca, R. M.: Evaluating the contribution of changes in isoprene emissions to surface ozone trends over the eastern United States, *J. Geophys. Res.*, 110, D12303, doi:10.1029/2004JD005485, 2005.

Gårdfeldt, K., Sommar, J., Strömberg, D., and Feng, X.: Oxidation of atomic mercury by hydroxyl radicals and photoinduced decomposition of methylmercury in the aqueous phase, *Atmos. Environ.*, 35, 3039–3047, 2001.

Gildemiester, A. E.: Urban atmospheric mercury, Ph. D., University of Michigan, Ann Arbor, 2001.

Goodsite, M. E., Plane, J. M. C., and Skov, H.: A theoretical study of the oxidation of Hg⁰ to HgBr₂ in the troposphere, *Environ. Sci. Technol.*, 38, 1772–1776, 2004.

Guentzel, J. L., Landing, W. M., Gill, G. A., and Pollman, C. D.: Processes influencing rainfall deposition of mercury in Florida, *Environ. Sci. Technol.*, 35, 863–873, 2001.

Gustin, M. and Jaffe, D. A.: Reducing the uncertainty in measurement and understanding of mercury in the atmosphere, *Environ. Sci. Technol.*, 44, 2222–2227, 2010.

Gustin, M. S., Taylor Jr., G. E., and Maxey, R. A.: Effect of temperature and air movement on the flux of elemental mercury from substrate to the atmosphere, *J. Geophys. Res.*, 102,

3891–3898, 1997.

Holmes, C. D., Jacob, D. J., Mason, R. P., and Jaffe, D. A.: Sources and deposition of reactive gaseous mercury in the marine atmosphere, *Atmos. Environ.*, 43, 2278–2285, 2009.

Holmes, C. D., Jacob, D. J., Corbitt, E. S., Mao, J., Yang, X., Talbot, R., and Slemr, F.: Global atmospheric model for mercury including oxidation by bromine atoms, *Atmos. Chem. Phys.*, 10, 12037–12057, doi:10.5194/acp-10-12037-2010, 2010.

Jacob, D. J., Crawford, J. H., Maring, H., Clarke, A. D., Dibb, J. E., Emmons, L. K., Ferrare, R. A., Hostetler, C. A., Russell, P. B., Singh, H. B., Thompson, A. M., Shaw, G. E., McCauley, E., Pederson, J. R., and Fisher, J. A.: The Arctic Research of the Composition of the Troposphere from Aircraft and Satellites (ARCTAS) mission: design, execution, and first results, *Atmos. Chem. Phys.*, 10, 5191–5212, doi:10.5194/acp-10-5191-2010, 2010.

Keeler, G. J., Landis, M. S., Norris, G. A., Christianson, E. M., and Dvonch, J. T.: Sources of mercury wet deposition in eastern Ohio, USA, *Environ. Sci. Technol.*, 40, 5874–5881, 2006.

Kellerhals, M., Beauchamp, S., Belzer, W., Blanchard, P., Froude, F., Harvey, B., McDonald, K., Pilote, M., Poissant, L., Puckett, K., Schroeder, B., Steffen, A., and Tordon, R.: Temporal and spatial variability of total gaseous mercury in Canada: results from the Canadian Atmospheric Mercury Measurement Network (CAMNet), *Atmos. Environ.*, 37, 1003–1011, 2003.

Li, Q. B., Jacob, D. J., Park, R., Wang, Y. X., Heald, C. L., Hudman, R., Yantosca, R. M., Martin, R. V., and Evans, M.: North American pollution outflow and the trapping of convectively lifted pollution by upper-level anticyclone, *J. Geophys. Res.*, 110, D10301, doi:10.1029/2004JD005039, 2005.

Lin, C. J. and Pehkonen, S. O.: The chemistry of atmospheric mercury: a review, *Atmos. Environ.*, 33, 2067–2079, 1999.

Lin, X. and Tao, Y.: A numerical modelling study on regional mercury budget for eastern North America, *Atmos. Chem. Phys.*, 3, 535–548, doi:10.5194/acp-3-535-2003, 2003.

Lindberg, S., Bullock, R., Ebinghaus, R., Engstrom, D., Feng, X. B., Fitzgerald, W., Pirrone, N., Prestbo, E., and Seigneur, C.: A Synthesis of Progress and Uncertainties in Attributing the Sources of Mercury in Deposition, *Ambio*, 36, 19–32, 2007.

Liu, H., Jacob, D., Bey, I., and Yantosca, R. M.: Constraints from Pb210 and Be7 on wet deposition and transport in a global three-dimensional chemical tracer model driven by assimilated meteorological fields, *J. Geophys. Res.*, 106, 12109–12128, doi:10.1029/2000JD900839, 2001.

ACPD

12, 2603–2646, 2012

Nested-grid simulation of mercury over North America

Y. Zhang et al.

Title Page

Abstract

Introduction

Conclusions

References

Tables

Figures

⏪

⏩

◀

▶

Back

Close

Full Screen / Esc

Printer-friendly Version

Interactive Discussion

Nested-grid simulation of mercury over North America

Y. Zhang et al.

Title Page

Abstract

Introduction

Conclusions

References

Tables

Figures

⏪

⏩

◀

▶

Back

Close

Full Screen / Esc

Printer-friendly Version

Interactive Discussion



- Lyman, S. N. and Gustin, M. S.: Speciation of atmospheric mercury at two sites in northern Nevada, USA, *Atmos. Environ.*, 42, 927–939, 2008.
- Lyman, S. N., Gustin, M. S., Prestbo, E. M., and Marsik, F. J.: Estimation of dry deposition of atmospheric mercury in Nevada by direct and indirect methods, *Environ. Sci. Technol.*, 41, 1970–1976, 2007.
- Lynch, J. A., Horner, K. S., and Grimm, J. W.: Atmospheric deposition: spatial and temporal variations in Pennsylvania 2002, Penn State Institutes of the Environment, The Pennsylvania State University, University Park, PA, 2003.
- Mao, H., Talbot, R. W., Sive, B. C., Youn Kim, S., Blake, D. R., and Weinheimer, A. J.: Arctic mercury depletion and its quantitative link with halogens, *J. Atmos. Chem.*, 65, 145–170, 2011.
- Mari, C., Jacob, D. J., and Bechtold, P.: Transport and scavenging of soluble gases in a deep convective cloud, *J. Geophys. Res.*, 105, 22255–22267, 2000.
- Mason, R. A.: Mercury emissions from natural processes and their importance in the global mercury cycle, in: *Mercury fate and transport in the global atmosphere: emissions, measurements and models*, edited by: Pirrone, N. and Mason, R. A., Springer, Dordrecht Heidelberg London New York, 173–191, 2009.
- MDN, National Atmospheric Deposition Program, Mercury Deposition Network Information, available at: <http://nadp.sws.uiuc.edu/mdn/>, last access: October 2011.
- Mergler, D., Anderson, H. A., Chan, L. H. M., Mahaffey, K. R., Murray, M., Sakamoto, M., and Stern, A. H.: Methylmercury exposure and health effects in humans: A worldwide concern, *Ambio*, 36, 3–11, 2007.
- Morel, F. M., Kraepiel, A. M. L., and Amyot, M.: The chemical cycle and bioaccumulation of mercury, *Annu. Rev. Ecol. Syst.*, 29, 543–566, 1998.
- Pacyna, E. G., Pacyna, J. M., Sundseth, K., Munthe, J., Kindbom, K., Wilson, S., Steenhuisen, F., and Maxson, P.: Global emission of mercury to the atmosphere from anthropogenic sources in 2005 and projections to 2020, *Atmos. Environ.*, 44, 2487–2499, 2010.
- Pan, L., Chai, T. F., Carmichael, G. R., Tang, Y. H., Streets, D., Woo, J. H., Friedli, H. R., and Radke, L. F.: Top-down estimate of mercury emissions in China using four-dimensional variational data assimilation, *Atmos. Environ.*, 41, 2804–2819, 2007.
- Park, R. J., Jacob, D. J., Kumar, N., and Yantosca, R. M.: Regional visibility statistics in the United States: Natural and transboundary pollution influences, and implications for the Regional Haze Rule, *Atmos. Environ.*, 40, 5405–5423, 2006.

**Nested-grid
simulation of
mercury over North
America**

Y. Zhang et al.

[Title Page](#)[Abstract](#)[Introduction](#)[Conclusions](#)[References](#)[Tables](#)[Figures](#)[⏪](#)[⏩](#)[◀](#)[▶](#)[Back](#)[Close](#)[Full Screen / Esc](#)[Printer-friendly Version](#)[Interactive Discussion](#)

Prestbo, E. M. and Gay, D. A.: Wet deposition of mercury in the US and Canada, 1996–2005: Results and analysis of the NADP mercury deposition network (MDN), *Atmos. Environ.*, 43, 4223–4233, 2009.

Rutter, A. P. and Schauer, J. J.: The effect of temperature on the gas-particle partitioning of reactive mercury in atmospheric aerosols, *Atmos. Environ.*, 41, 8647–8657, 2007.

Seigneur, C., Karamchandani, P., Lohman, K., Vijayaraghavan, K., and Shia, R. L.: Multiscale modeling of the atmospheric fate and transport of mercury, *J. Geophys. Res.*, 106, 27795–27809, 2001.

Seigneur, C., Vijayaraghavan, K., Lohman, K., Karamchandani, P., and Scott, C.: Global source attribution for mercury deposition in the United States, *Environ. Sci. Technol.*, 38, 555–569, 2004.

Selin, N. E. and Jacob, D. J.: Seasonal and spatial patterns of mercury wet deposition in the United States: Constraints on the contribution from North American anthropogenic sources, *Atmos. Environ.*, 42, 5193–5204, 2008.

Selin, N. E., Jacob, D. J., Park, R. J., Yantosca, R. M., Strode, S., Jaegle, L., and Jaffe, D.: Chemical cycling and deposition of atmospheric mercury: Global constraints from observations, *J. Geophys. Res.*, 112, D02308, doi:10.1029/2006jd007450, 2007.

Selin, N. E., Jacob, D. J., Yantosca, R. M., Strode, S., Jaegle, L., and Sunderland, E. M.: Global 3-D land-ocean-atmosphere model for mercury: Present-day versus preindustrial cycles and anthropogenic enrichment factors for deposition, *Global Biogeochem. Cy.*, 22, GB2011, doi:10.1029/2007gb003040, 2008.

Shia, R. L., Seigneur, C., Pai, P., Ko, M., and Sze, N. D.: Global simulation of atmospheric mercury concentrations and deposition fluxes, *J. Geophys. Res.*, 104, 23747–23760, 1999.

Si, L. and Ariya, P. A.: Reduction of oxidized mercury species by dicarboxylic acids (C-2-C-4): Kinetic and product studies, *Environ. Sci. Technol.*, 42, 5150–5155, 2008.

Simpson, W. R., Carlson, D., Hnninger, G., Douglas, T. A., Sturm, M., Perovich, D., and Platt, U.: First-year sea-ice contact predicts bromine monoxide (BrO) levels at Barrow, Alaska better than potential frost flower contact, *Atmos. Chem. Phys.*, 7, 621–627, doi:10.5194/acp-7-621-2007, 2007.

Soerensen, A. L., Sunderland, E. M., Holmes, C. D., Jacob, D. J., Yantosca, R. M., Skov, H., Christensen, J. H., Strode, S. A., and Mason, R. P.: An Improved Global Model for Air-Sea Exchange of Mercury: High Concentrations over the North Atlantic, *Environ. Sci. Technol.*, 44, 8574–8580, 2010.

Nested-grid simulation of mercury over North America

Y. Zhang et al.

Title Page

Abstract

Introduction

Conclusions

References

Tables

Figures

⏪

⏩

◀

▶

Back

Close

Full Screen / Esc

Printer-friendly Version

Interactive Discussion

- Steffen, A., Douglas, T., Amyot, M., Ariya, P., Aspmo, K., Berg, T., Bottenheim, J., Brooks, S., Cobbett, F., Dastoor, A., Dommergue, A., Ebinghaus, R., Ferrari, C., Gardfeldt, K., Goodsite, M. E., Lean, D., Poulain, A. J., Scherz, C., Skov, H., Sommar, J., and Temme, C.: A synthesis of atmospheric mercury depletion event chemistry in the atmosphere and snow, *Atmos. Chem. Phys.*, 8, 1445–1482, doi:10.5194/acp-8-1445-2008, 2008.
- Strahan, S. E., Duncan, B. N., and Hoor, P.: Observationally derived transport diagnostics for the lowermost stratosphere and their application to the GMI chemistry and transport model, *Atmos. Chem. Phys.*, 7, 2435–2445, doi:10.5194/acp-7-2435-2007, 2007.
- Streets, D. G., Zhang, Q., and Wu, Y.: Projections of global mercury emissions in 2050, *Environ. Sci. Technol.*, 43, 2983–2988, 2009.
- Strode, S. A., Jaeglé, L., Selin, N. E., Jacob, D. J., Park, R. J., Yantosca, R. M., Mason, R. P., and Slemr, F.: Air-sea exchange in the global mercury cycle, *Global Biogeochem. Cy.*, 21, GB1017, doi:10.1029/2006GB002766, 2007.
- Sunderland, E. M.: Mercury exposure from domestic and imported estuarine and marine fish in the U.S. seafood market, *Environ. Health Perspect.*, 115, 235–242, 2007.
- Temme, C., Slemr, F., Ebinghaus, R., and Einax, J. W.: Distribution of mercury over the Atlantic Ocean in 1996 and 1999–2001, *Atmos. Environ.*, 37, 1889–1897, 2003.
- Temme, C., Blanchard, P., Steffen, A., Banic, C., Beauchamp, S., Poissant, L., Tordon, R., and Wiens, B.: Trend, seasonal and multivariate analysis study of total gaseous mercury data from the Canadian atmospheric mercury measurement network (CAMNet), *Atmos. Environ.*, 41, 5423–5441, 2007.
- ter Schure, A., Caffrey, J., Gustin, M., Holmes, C., Hynes, A., Landing, B., Landis, M., Laudel, D., Levin, L., Nair, U., Jansen, J., Ryan, J., Walters, J., Schauer, J., Volkamer, R., Waters, D., and Weiss, P.: An integrated approach to assess elevated mercury wet deposition and concentrations in the southeastern United States, 10th International Conference on Mercury as Global Pollutant, Halifax, Nova Scotia, Canada, 2011.
- Vijayaraghavan, K., Karamchandani, P., Seigneur, C., Balmori, R., and Chen, S.-Y.: Plume-in-grid modeling of atmospheric mercury, *J. Geophys. Res.*, 113, D24305, doi:10.1029/2008jd010580, 2008.
- Wang, Q., Jacob, D. J., Fisher, J. A., Mao, J., Leibensperger, E. M., Carouge, C. C., Le Sager, P., Kondo, Y., Jimenez, J. L., Cubison, M. J., and Doherty, S. J.: Sources of carbonaceous aerosols and deposited black carbon in the Arctic in winter-spring: implications for radiative forcing, *Atmos. Chem. Phys.*, 11, 12453–12473, doi:10.5194/acp-11-12453-2011, 2011.

Nested-grid simulation of mercury over North America

Y. Zhang et al.

Title Page

Abstract

Introduction

Conclusions

References

Tables

Figures

⏪

⏩

◀

▶

Back

Close

Full Screen / Esc

Printer-friendly Version

Interactive Discussion



- Wang, Y. X., McElroy, M. B., Wang, T., and Palmer, P. I.: Asian emissions of CO and NO_x: Constraints from aircraft and Chinese station data, *J. Geophys. Res.*, 109, D24304, doi:10.1029/2004JD005250, 2004a.
- 5 Wang, Y. X., McElroy, M. B., Jacob, D. J., and Yantosca, R. M.: A nested grid formulation for chemical transport over Asia: Applications to CO, *J. Geophys. Res.*, 109, D22307, doi:10.1029/2004jd005237, 2004b.
- Weiss-Penzias, P. S., Gustin, M. S., and Lyman, S. N.: Sources of gaseous oxideized mercury and mercury dry deposition at two southeastern U.S. sites, *Atmos. Environ.*, 45, 4569–4579, 2011.
- 10 Wesely, M. L.: Parameterization of surface resistances to gaseous dry deposition in regional-scale numerical-models, *Atmos. Environ.*, 23, 1293–1304, 1989.
- White, E. M., Keeler, G. J., and Landis, M. S.: Spatial variability of mercury wet deposition in eastern Ohio: summertime meteorological case study analysis of local source influences, *Environ. Sci. Technol.*, 43, 4946–4953, 2009.
- 15 Yang, X., Cox, R. A., Warwick, N. J., Pyle, J. A., Carver, G. D., O'Connor, F. M., and Savage, N. H.: Tropospheric bromine chemistry and its impacts on ozone: A model study, *J. Geophys. Res.*, 110, D23311, doi:10.1029/2005JD006244, 2005.

Nested-grid simulation of mercury over North America

Y. Zhang et al.

Table 1. Comparison of annual wet deposition fluxes (2008–2009) between MDN observations and the nested-grid GEOS-Chem model.

Regions ^a	# of sites	Annual precipitation (cm yr ⁻¹) ^b		Annual Hg wet deposition flux (μg m ⁻² yr ⁻¹)		
		MDN	GEOS-5	MDN Observations	GEOS-Chem STD simulation	GEOS-Chem IPR simulation
MW	19	6.2±2.6	5.8±1.7	7.0±4.8	5.9±2.3 (–15 % ^c)	4.9±2.3 (–28 %)
NE	10	9.9±1.7	9.5±1.6	6.8±3.0	6.8±2.4 (+2.6 %)	5.9±2.3 (–11 %)
ORV	29	9.1±1.9	9.3±1.8	9.3±3.6	11±4.5 (+27 %)	8.9±3.7 (+3.4 %)
SE	20	11±2.9	10±5.2	13±5.3	11±5.4 (–14 %)	10±5.1 (–20 %)
All sites	95	8.1±1.3	8.1±1.5	8.8±3.6	8.3±3.4 (+3.4 %)	7.1±3.1 (–18 %)

The model is sampled at the location of the 95 sites selected.

^a Regions are defined in Fig. 2.

^b Mean and standard deviation of monthly averaged values.

^c The mean normalized bias, defined as the mean of $\frac{\text{model-observation}}{\text{observation}} \times 100$ is indicated in parentheses.

Title Page

Abstract

Introduction

Conclusions

References

Tables

Figures

⏪

⏩

◀

▶

Back

Close

Full Screen / Esc

Printer-friendly Version

Interactive Discussion

Nested-grid simulation of mercury over North America

Y. Zhang et al.

Title Page

Abstract

Introduction

Conclusions

References

Tables

Figures

⏪

⏩

◀

▶

Back

Close

Full Screen / Esc

Printer-friendly Version

Interactive Discussion

Table 2. Contribution from North American Hg anthropogenic sources to wet and dry deposition (2008–2009).

Regions		GEOS-Chem STD simulation	GEOS-Chem IPR simulation
MW	Wet	31 %	15 %
	Dry	21 %	14 %
	Total	24 %	14 %
NE	Wet	32 %	16 %
	Dry	18 %	12 %
	Total	23 %	13 %
ORV	Wet	32 %	15 %
	Dry	41 %	24 %
	Total	39 %	22 %
SE	Wet	16 %	8 %
	Dry	25 %	16 %
	Total	23 %	13 %
Contiguous US	Wet	22 %	10 %
	Dry	20 %	13 %
	Total	21 %	12 %

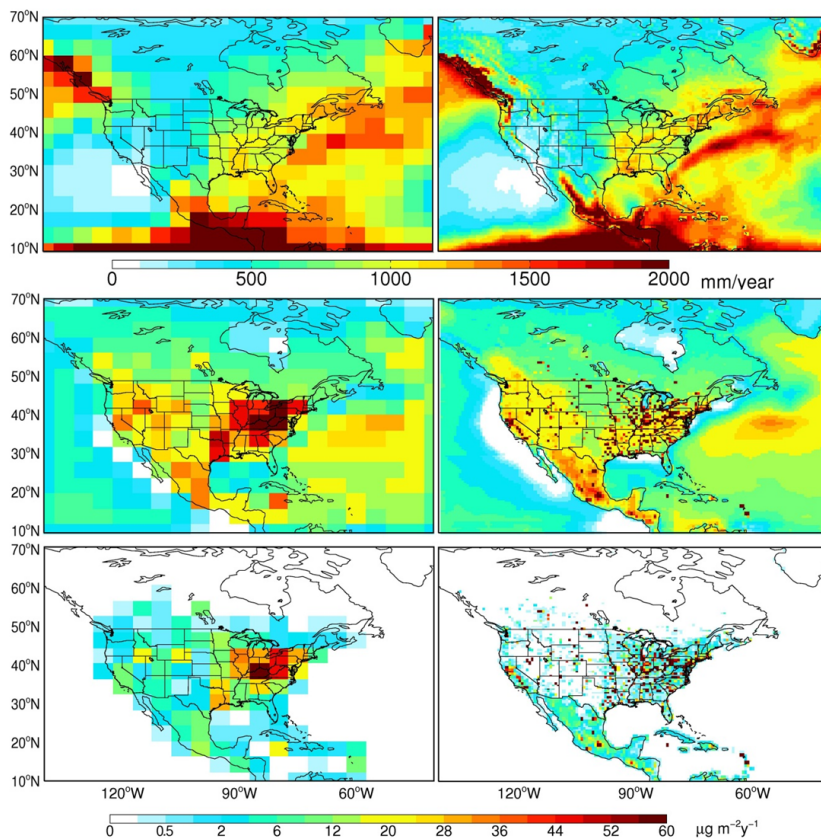


Fig. 1. Comparison between the global ($4 \times 5^\circ$, left column) and nested ($1/2 \times 2/3^\circ$, right column) models over the North American domain. Top row: total surface precipitation in 2008. Middle row: total Hg emissions including natural and anthropogenic sources (IPR simulation). Bottom row: anthropogenic Hg emissions based on the EPA NEI 2005 inventory for the US, the NPRI 2005 inventory for Canada, and the GEIA2005 inventory for Mexico.

Nested-grid simulation of mercury over North America

Y. Zhang et al.

Title Page

Abstract Introduction

Conclusions References

Tables Figures

◀ ▶

◀ ▶

Back Close

Full Screen / Esc

Printer-friendly Version

Interactive Discussion



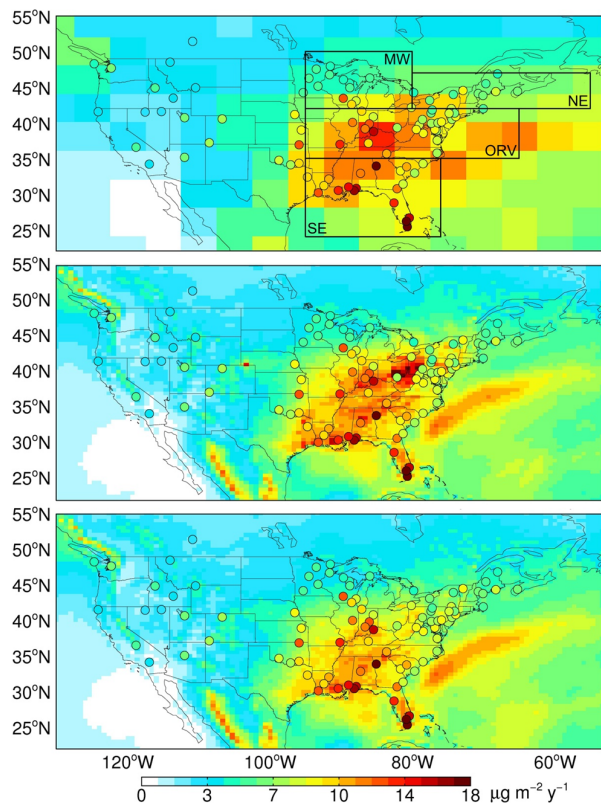


Fig. 2. Annual mean observed (circle) and simulated (background) Hg wet deposition flux for 2008–2009 over North America. Observations are from the Mercury Deposition Network (MDN). The three panels correspond to different GEOS-Chem Hg simulations: global STD model (top), nested STD simulation (middle), nested IPR simulation (bottom). The four regions considered in this study are indicated with black boxes in the top panel: Midwest (MW), Northeast (NE), Ohio River Valley (ORV), and Southeast (SE).

Nested-grid simulation of mercury over North America

Y. Zhang et al.

Title Page	
Abstract	Introduction
Conclusions	References
Tables	Figures
◀	▶
◀	▶
Back	Close
Full Screen / Esc	
Printer-friendly Version	
Interactive Discussion	



Nested-grid simulation of mercury over North America

Y. Zhang et al.

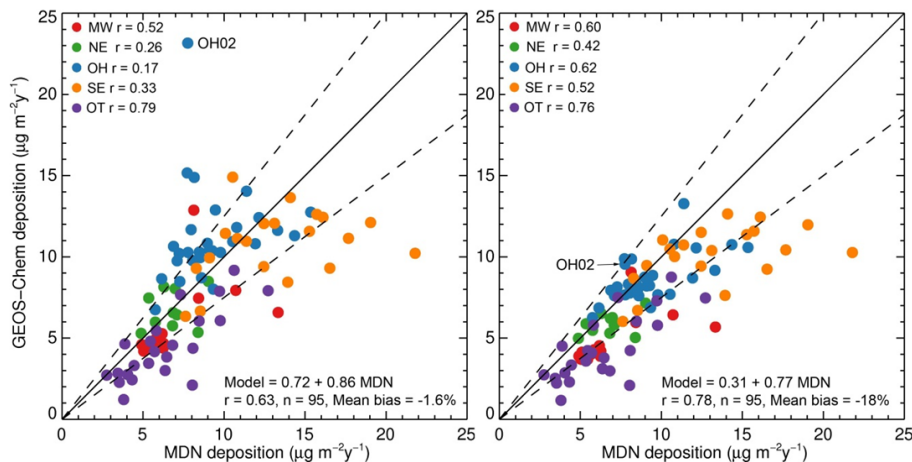


Fig. 3. Scatter plot of observed and modeled annual mean (2008–2009) Hg wet deposition flux. Left panel: standard nested-grid simulation; Right panel: IPR nested-grid simulation. The solid line indicates the 1:1 line, while the dashed lines correspond to $\pm 25\%$. The points are colored according to their geographic location as defined in Fig. 2 (OT corresponds to sites west of 95° W longitude). The correlation coefficient for each region as well as the overall regression statistics are also shown.

[Title Page](#)
[Abstract](#)
[Introduction](#)
[Conclusions](#)
[References](#)
[Tables](#)
[Figures](#)
[⏪](#)
[⏩](#)
[◀](#)
[▶](#)
[Back](#)
[Close](#)
[Full Screen / Esc](#)
[Printer-friendly Version](#)
[Interactive Discussion](#)

Nested-grid simulation of mercury over North America

Y. Zhang et al.

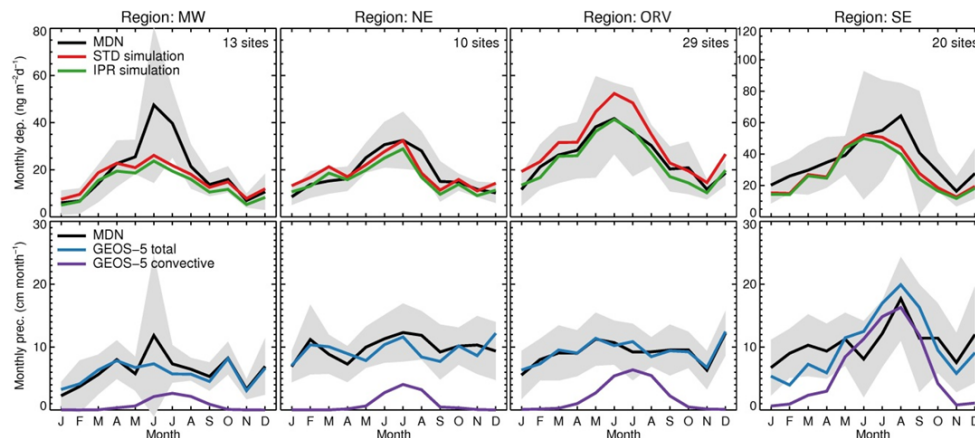


Fig. 4. Monthly mean variation in Hg wet deposition fluxes ($\text{ng m}^{-2} \text{d}^{-1}$) and precipitation (cm month^{-1}) averaged over 2008–2009 for four regions over the eastern United States. Top row: MDN observations (black line, with shaded area indicating the standard error) are compared to the STD nested (red line) and the IPR nested-grid (green line) simulations. Bottom row: surface precipitation observed at MDN sites is compared to total and convective GEOS-5 precipitation.

Title Page

Abstract

Introduction

Conclusions

References

Tables

Figures

◀

▶

◀

▶

Back

Close

Full Screen / Esc

Printer-friendly Version

Interactive Discussion

Nested-grid simulation of mercury over North America

Y. Zhang et al.

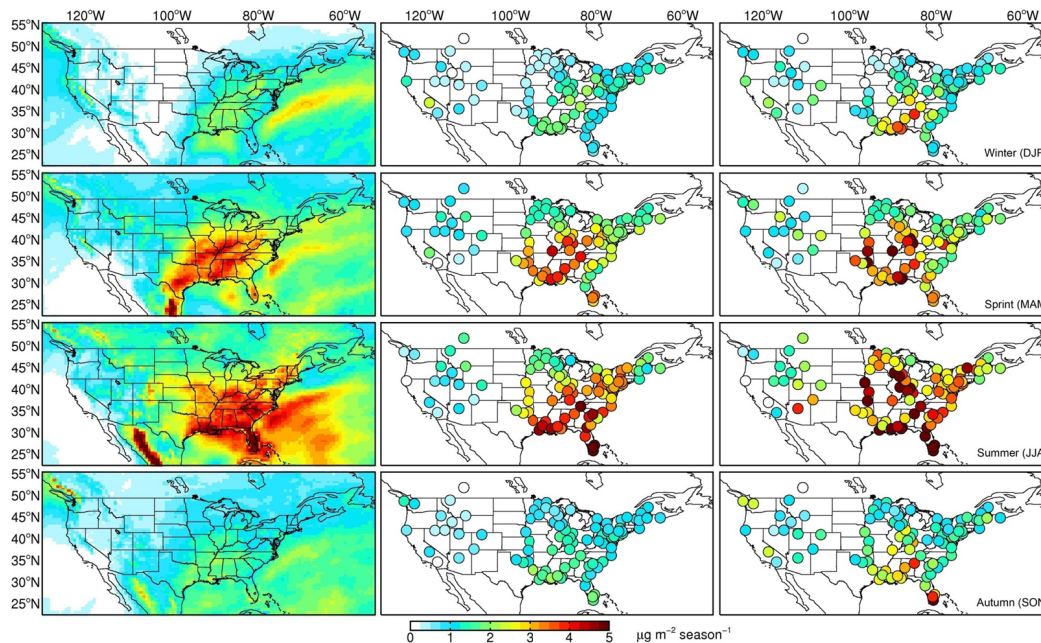


Fig. 5. Seasonal variations in the Hg wet deposition flux for 2008–2009. From top to bottom: winter (DJF), spring (MAM), summer (JJA), and autumn (SON). The first column shows the spatial distribution of the IPR nested-grid model wet deposition; the second column shows the model values extracted at MDN sites; the third column shows the observed wet deposition at MDN sites.

Title Page

Abstract

Introduction

Conclusions

References

Tables

Figures

◀

▶

◀

▶

Back

Close

Full Screen / Esc

Printer-friendly Version

Interactive Discussion

Nested-grid simulation of mercury over North America

Y. Zhang et al.

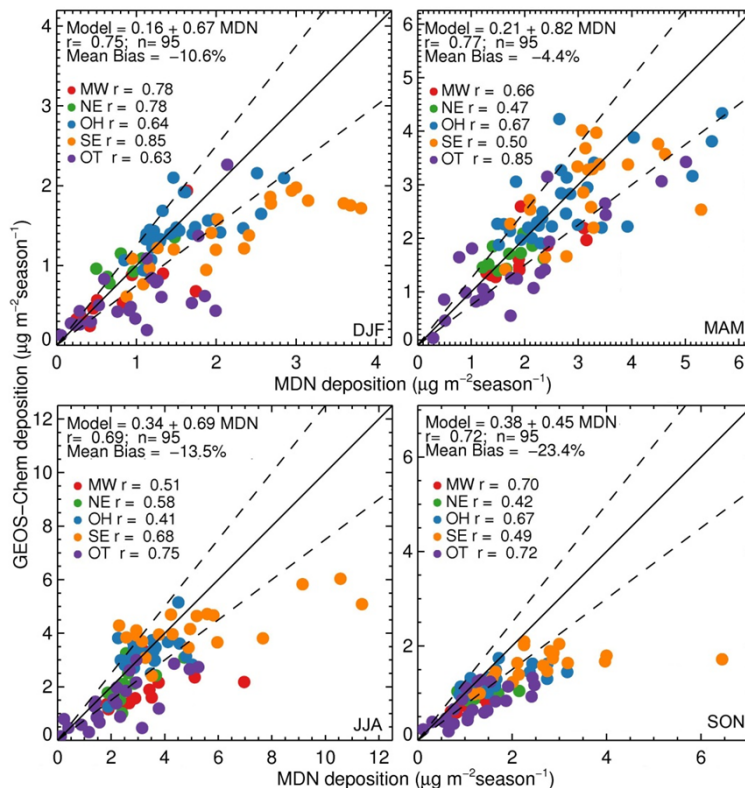


Fig. 6. Scatter plot of seasonal averaged (2008–2009) Hg wet deposition fluxes ($\mu\text{g m}^{-2}\text{season}^{-1}$) between IPR nested-grid simulation (vertical axis) and MDN observations (horizontal axis). Different colors denote sites in different regions as defined in Fig. 2, while OT corresponds to sites west of 95° W longitude.

Title Page

Abstract

Introduction

Conclusions

References

Tables

Figures

◀

▶

◀

▶

Back

Close

Full Screen / Esc

Printer-friendly Version

Interactive Discussion

Nested-grid simulation of mercury over North America

Y. Zhang et al.

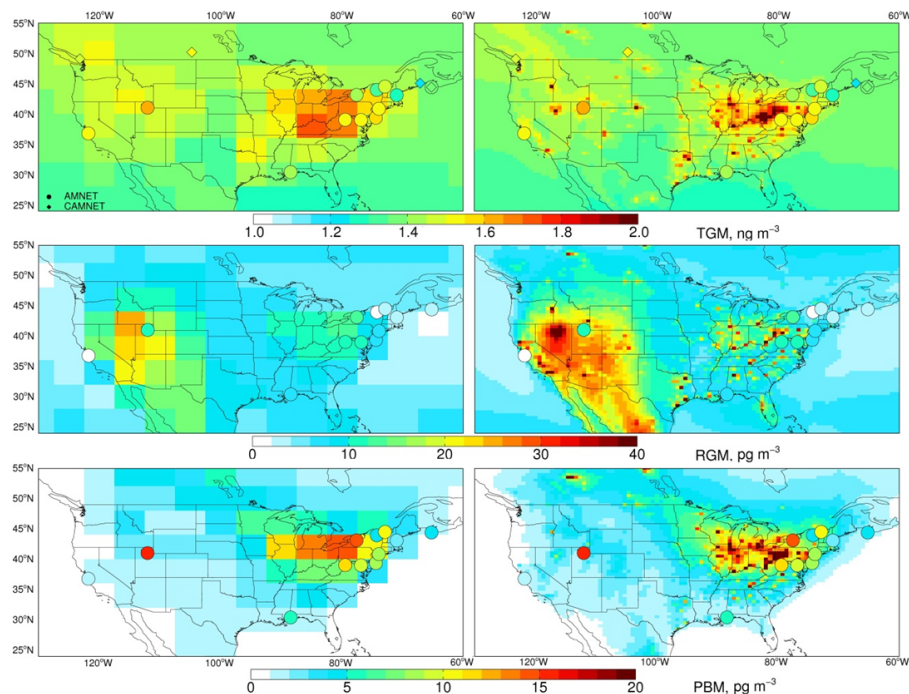


Fig. 7. Annual mean surface concentrations of TGM (top), RGM (middle) and PBM (bottom) during 2008–2009. Results from the global (left column) and nested (right column) IPR simulations are compared to observations from 14 AMNET sites (circles) and 5 CAMNET sites (diamonds). Two pairs of AMNet sites are collocated, so only 12 AMNet sites are identifiable.

[Title Page](#)[Abstract](#)[Introduction](#)[Conclusions](#)[References](#)[Tables](#)[Figures](#)[◀](#)[▶](#)[◀](#)[▶](#)[Back](#)[Close](#)[Full Screen / Esc](#)[Printer-friendly Version](#)[Interactive Discussion](#)

Nested-grid simulation of mercury over North America

Y. Zhang et al.

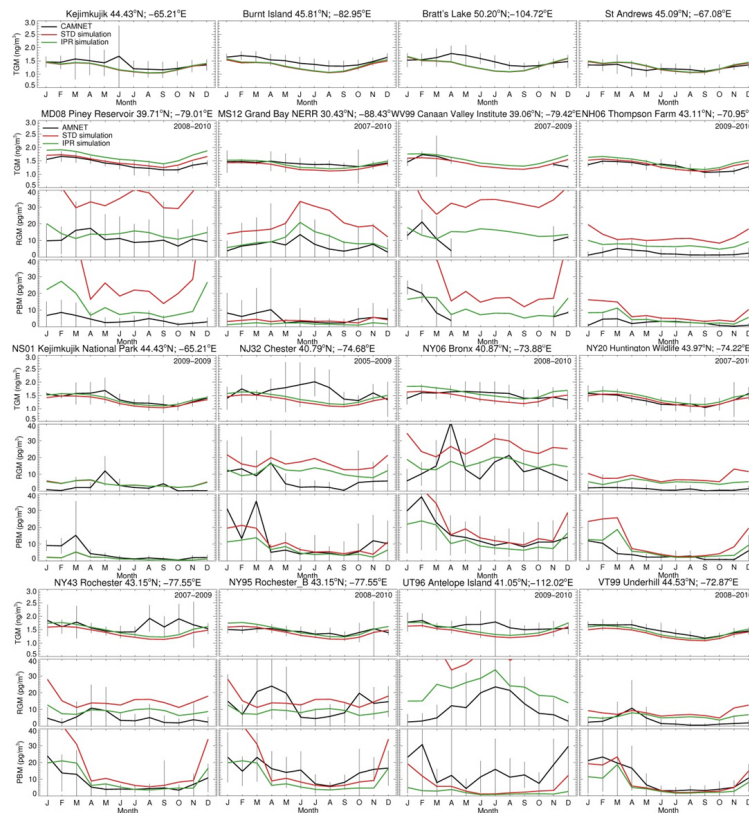


Fig. 8. Comparison of the monthly mean TGM, RGM and PBM concentrations observed at CAMNet and AMNet sites with the STD (red line) and IPR (green line) nested-grid GEOS-Chem simulations. The CAMNet sites are averaged over 2004–2007, while the AMNet sites observations are averaged during 2005–2010 when observation are available. The model results are averaged over 2008–2009. For the CAMNet sites (the 4 panels in the first row), only TGM observations are available.

Title Page

Abstract

Introduction

Conclusions

References

Tables

Figures

◀

▶

◀

▶

Back

Close

Full Screen / Esc

Printer-friendly Version

Interactive Discussion



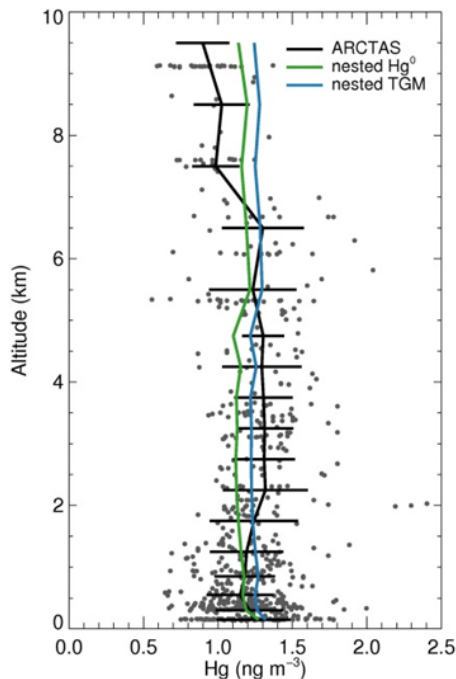


Fig. 9. Mean vertical profiles (black line) and standard deviations of TGM concentrations measured during the ARCTAS campaign over California and Nevada (32–43° N; 114–125° W) during summer 2008. Gray points correspond to individual TGM observations. The modeled vertical profile of Hg^0 from the nested IPR simulation is shown in green, while modeled TGM is in blue. The model is sampled at the time of observations along the flight track.

Nested-grid simulation of mercury over North America

Y. Zhang et al.

Title Page	
Abstract	Introduction
Conclusions	References
Tables	Figures
◀	▶
◀	▶
Back	Close
Full Screen / Esc	
Printer-friendly Version	
Interactive Discussion	



Nested-grid simulation of mercury over North America

Y. Zhang et al.

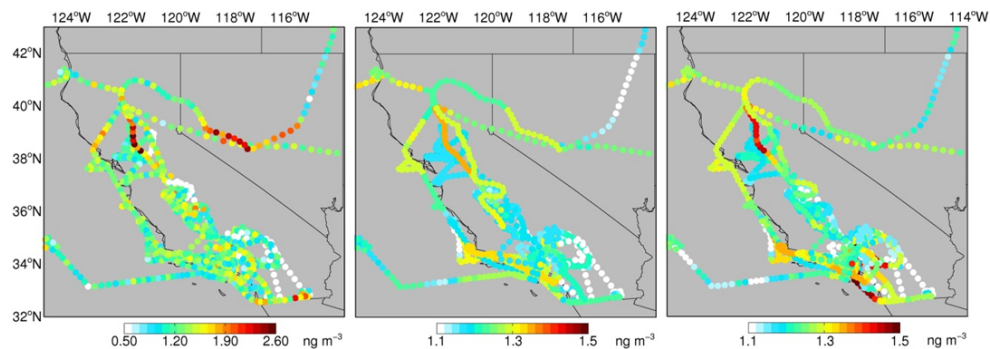


Fig. 10. Observed TGM concentrations during the ARCTAS aircraft campaign (left). The TGM concentrations predicted by the global (middle) and nested (right) IPR simulations sampled along the flight track are also shown. Note that the observation and model results have different color scales.

[Title Page](#)[Abstract](#)[Introduction](#)[Conclusions](#)[References](#)[Tables](#)[Figures](#)[⏪](#)[⏩](#)[◀](#)[▶](#)[Back](#)[Close](#)[Full Screen / Esc](#)[Printer-friendly Version](#)[Interactive Discussion](#)

Nested-grid simulation of mercury over North America

Y. Zhang et al.

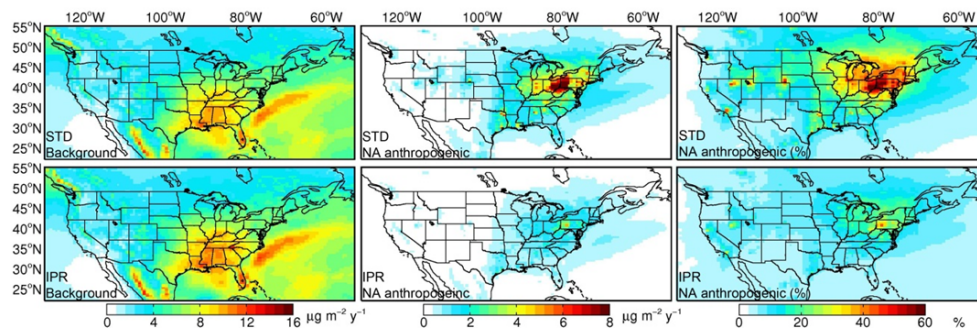


Fig. 11. Contributions of global background and North American anthropogenic emissions to wet deposition during 2008–2009. Top row (STD simulation): absolute wet deposition fluxes due to global background (left) and North American anthropogenic sources (middle), and the percent contribution by North American anthropogenic sources (right). The bottom three panels are for the IPR simulation.

[Title Page](#)[Abstract](#)[Introduction](#)[Conclusions](#)[References](#)[Tables](#)[Figures](#)[◀](#)[▶](#)[◀](#)[▶](#)[Back](#)[Close](#)[Full Screen / Esc](#)[Printer-friendly Version](#)[Interactive Discussion](#)